Northumbria Research Link

NH₄Cl-assisted preparation of single Ni sites anchored carbon nanosheet catalysts for highly <mark>efficient</mark> carbon dioxide electroreduction

Dan Ping[a], Feng Yi[a], Guiwei Zhang[a], Shide Wu*[,a], Shaoming Fang[a,*], Kailong Hu[b], Ben Bin Xu[c], Junna Ren[d], Zhanhu Guo[e,*]

[a] Henan Provincial Key Laboratory of Surface & Interface Science, Henan Engineering Research Center of Chemical Engineering Separation Process Intensification, School of Material and Chemical Engineering, Zhengzhou University of Light Industry, Zhengzhou 450002, China

[b] School of Materials Science and Engineering, Harbin Institute of Technology, Shenzhen 518055, China

[c] Mechanical and Construction Engineering, Faculty of Engineering and Environment, Northumbria University, Newcastle Upon Tyne, NE1 8ST, UK

[d] College of Materials Science and Engineering, Taiyuan University of Science and Technology, Taiyuan, 030024, China

[e] Integrated Composites Lab (ICL), Department of Chemical & Biomolecular Engineering, University of Tennessee, Knoxville, TN, 37996, USA

E-Mail: wushide@zzuli.edu.cn (S. Wu); smfang@zzuli.edu.cn (S. Fang); and nanomaterials2000@gmail.com (Z. Guo)

Abstract: Single-atomic transition metal-nitrogen codoped carbon (M-N-C) are efficient substitute catalysts for noble metals to catalyze electrochemical CO_2 reduction reaction. However, the uncontrolled aggregations of metal and serious loss of nitrogen species constituting the M-Nx active sites are frequently observed in the commonly used pyrolysis procedure. Herein, single-atomic nickel (Ni)-based sheet-like electrocatalysts with abundant Ni-N4 active sites were created by using a novel ammonium chloride (NH4Cl)-assited pyrolysis method. Spherical aberration correction electron microscopy and X-ray absorption fine structure analysis clearly revealed that Ni species are atomically dispersed and anchored by N in Ni-N4 structure. The addition of <mark>ammonium chloride (NH4Cl)</mark> optimized the mesopore size to 7-10 nm, and increased the concentrations of pyridinic N (3.54 wt%) and Ni-N4 (3.33 wt%) species. The synergistic catalytic effect derived from Ni-N4 active sites and pyridinic N species achieved an outstanding CO2RR performance, presenting a high CO Faradaic efficiency (FE_{CO}) up to 98% and a large CO partial current density of 8.5 mA·cm^{-2} at a low potential of -0.62 V *vs*. RHE. Particularly, the FE_{CO} maintains above 80% within a large potential range from -0.43 to -0.73 V *vs*. RHE. This work provides a practical and feasible approach to build highly active single-atomic catalysts for CO_2 <mark>conversion</mark> systems.

Keywords: CO_2 reduction; electrocatalyst; single-atomic Ni; NH4Cl; pyridinic N.

1. Introduction

The conversion of <mark>carbon dioxide (CO_2)</mark> to high value-added carbon products (such as CO, HCOOH, $CH_2=CH_2$, et al.) through electrochemical reduction reaction (CO_2RR) provides a feasible technology to alleviate the global warming and achieve the carbon neutrality [1, 2]. Among them, CO, which is an important feedstock for synthesizing various liquid carbon-based fuels via Fischer-Tropsch processis [3, 4], is recognized as the particularly desired product. However, CO_2RR often suffers from high <mark>overpotentials</mark>, insufficient efficiency and unsatisfactory stability owing to the high stability of CO_2 and the competitive hydrogen evolution reaction [5, 6]. In this regard, the development of highly effective, selective, and stable electrocatalysts are quite essential to facilitate CO_2RR.

Noble metals, such as Au [7], Pd [8] and Ag [9], are currently the most active catalysts for CO_2RR. Nevertheless, their high cost and limited reserves greatly constrain the practical applications. Therefore, developing earth-abundant catalysts with adequate activity and selectivity is still the primary task for improving the overall economics of CO_2RR. Recently, single atom catalysts with atomically dispersed transition metal anchored on N-doped carbon (M-N-C) have demonstrated great potential for CO_2RR to CO on account of their maximum atom utilization and high efficiency [10-12]. Typically, single metal atoms coordinated with N atoms ($M-N_X$) in M-N-C catalysts were reported to be the main active sites for CO_2RR [13-15]. At the same time, pyridinic N is also a favorable site for CO production among various types of N species (such as pyridinic N,

pyrrolic N, graphitic N and oxidized N) [16]. However, M-Nx species frequently suffer from uncontrolled metal aggregations and serious N loss in the commonly used pyrolysis process [17, 18], resulting in the performance degradation.

Considerable efforts have been devoted to suppress the metal migrations and N release for boosting electrocatalytic reactions [19, 20], including optimizing metal precursors [21, 22], incorporating additional heteroatoms [23-25] and coating protective carbon layers [26, 27]. Particularly, the carbon layer coating process, which could effectively inhibit the migrations of metal atoms and preserve the M-Nx sites, has attracted increasing attention in the preparation of single-atom catalysts. For instance, Li et al. [26] have successfully prepared exclusive Ni-N$_4$ structures by using carbon layer coating outside the Ni-doped g-C$_3$N$_4$ precursor. Lou et al. [25] have constructed a hollow N-rich carbon with dense single Ni sites via a dual-linker zeolitic tetrazolate framework-engaged strategy, which showed remarkable performances for CO production. The dual-linker employment could provide rich N species for anchoring abundant Ni atoms. Despite these achievements, it is still imperative and challenging to construct satisfying M-N-C catalysts with high density of accessible active sites through a simple process.

Herein, we report a novel NH$_4$Cl-assited pyrolysis strategy to construct isolated single Ni atoms anchored on mesoporous ultrathin N-C nanosheets. Surprisingly, NH$_4$Cl co-pyrolysis plays a vital role in achieving increased concentrations of single Ni active sites (3.33 wt%) and pyridinic N species (3.54 wt%), and an optimized mesopore size

4

(7-10 nm). The synergistic effect of abundant Ni-Nx and pyridinic N endows the as-prepared catalyst with outstanding CO$_2$RR performance, i.e., 98% of CO faradaic efficiency and 8.5 mA·cm^{-2} of CO partial current density at a low potential of -0.62 V *vs*. RHE. The distribution and coordination structure of Ni species characterized by spherical aberration correction electron microscopy and X-ray absorption fine structure indicate that Ni species are atomically dispersed and anchored by N in the Ni-N$_4$ structure. The catalytic role of both Ni-Nx and pyridinic N sites are confirmed by a series of experiments. This work sheds a new light on the design of highly efficient M-N-C catalysts for practical applications.

2. Experimental

2.1. Reagents and Chemicals

All reagents were analytical grade and directly used without any additional treatment. Melamine (C$_3$H$_6$N$_6$, 99.5%), absolute ethyl alcohol (C$_2$H$_6$O, $\geqslant$99.7%) and sulfuric acid (H$_2$SO$_4$, 98.0%) were purchased from Damao chemical reagent factory. Glucose (C$_6$H$_{12}$O$_6$, 99.7%), nickel dichloride hexahydrate (NiCl$_2$·6H$_2$O, 98.0%) and ammonium chloride (NH$_4$Cl, 99.5%) were provided by Tianjin Fengchuan chemical regent technologies Co., Ltd. Potassium bicarbonate (KHCO$_3$, 99.99%) and potassium hydroxide (KOH, 95%) were obtained from Shanghai Macklin Biochemical Co., Ltd. Nafion solution (5 wt%) was purchased from Sigma-Aldrich Chemical Reagent Co., Ltd. All gases including N$_2$, Ar and CO$_2$ were of high purity (99.999%).

2.2. Sample preparation

The synthesis of g-C₃N₄ nanosheets: The g-C_3N_4 nanosheets were obtained by a thermal exfoliation method. 5 g of melamine was first calcined at 550 °C for 4 h at a ramping rate of 2 °C min^{-1}, and then calcined at 500 °C for 2 h at a ramping rate of 5 °C·min^{-1} in a muffle.

The synthesis of Ni-N-C-NH₄Cl catalysts: In a typical synthesis procedure, g-C_3N_4 (0.3 g), glucose (1.2 g), and $NiCl_2$·$6H_2O$ (0.258 g) were mixed in 30 mL deionized water, and stirred to obtain a homogenous mixture. Subsequently, the mixture was poured into a Teflon-lined stainless-steel autoclave and reacted at 160 °C for 10 h. After washing and drying, the Ni-g-C_3N_4@C intermediate was obtained. Next, the Ni-g-C_3N_4@C and NH_4Cl with the mass ratio of 2:1 was thoroughly mixed and heated at 900 °C for 2 h at a ramping rate of 5 °C min^{-1} in a N_2 atmosphere. To remove the remained metal particles and unstable species, the material was etched in 2 M H_2SO_4 at 80 °C for 5 h. Afterwards, the material was heated again at 900 °C for 1 h to acquire the final Ni-N-C-NH₄Cl catalyst.

The synthesis of Ni-N-C catalysts: The Ni-N-C catalyst was prepared via a similar process with the Ni-N-C-NH₄Cl catalyst except for no addition of NH_4Cl to validate the role of NH_4Cl.

The synthesis of N-C catalysts: The N-C catalyst was also prepared via a similar process with the Ni-N-C-NH₄Cl catalyst except for no addition of both $NiCl_2$·$6H_2O$ and NH_4Cl.

2.3. Materials characterization

The crystal structure of the catalysts was characterized by X-ray diffraction (XRD, Rigaku D/Max-2500) with Cu-Ka radiation. The morphology of the catalysts was examined by field emission scanning electron microscope (FESEM, JEOL JSM-7001F), transmission electron microscope (TEM, JEOL JEM-2100F) and aberration-corrected high-angle annular dark-field scanning transmission electron microscopy (AC-HAADF-STEM, FEI Titan3 Themis G2). The thickness of the samples was measured by atomic force microscopy (AFM, Bruker nanojnc). The specific surface area and pore size distribution of the catalysts were obtained from N_2 adsorption/desorption analyses (Micromeritics, ASAP 2010) using the Brunauer-Emmett-Teller (BET) and Barrett Joyner Halenda (BJH) methods, respectively. CO_2 temperature-programmed desorption (CO_2-TPD) was conducted on a Chemical adsorption instrument (Chemisorb 2720, China) equipped with a TCD detector. The metal content in samples was acquired through atomic absorption spectroscopy (AAS, ContrAA700) and X-ray photoelectron spectroscopy (XPS) spectra that were collected on the Escalab-250Xi using an Al Kα radiation. All the binding energies were referenced to the standard C1s peak at 284.6 eV in this experiment. The defect degree of catalysts was determined by Raman spectra (Renishaw, In Via). The in-situ X-ray absorption fine structure (XAFS) spectra at the Ni K-edge were conducted in a transmission mode at the beamline 12C of the Photon Factory (KEK, Japan). Both Ni foil and NiO were acted as standard control samples.

2.4. Electrochemical measurements

All electrochemical measurements were conducted with a CHI 760E

electrochemical workstation at room temperature and atmospheric pressure on a H-type

three-electrode cell. The electrolyte was CO_2-saturated 0.5 M $KHCO_3$ solution with the

pH of *ca.* 7.3. The sample-coated GCE was employed as the working electrode. The

Ag/AgCl electrode and the Pt plate were employed as reference and counter electrodes,

respectively. All potentials were converted to the reversible hydrogen electrode (RHE)

according to eq. (1). To prepare the catalyst ink, 5.0 mg of catalyst was dispersed in 30

μL 5% nafion and 970 μL ethanol, and then ultrasonicated for 1 h. An aliquot of 6 μL

catalyst ink was dropped onto a polished glassy carbon electrode, giving a mass loading

of 0.75 mg·cm^{-2}.

$$E(vs.\ RHE) = E(vs.\ Ag/AgCl) + 0.197 + 0.059 * pH \qquad (1)$$

The linear sweep voltammetry (LSV) curves were conducted at a scan rate of 5

mV·s^{-1}. All current densities were corrected according to the geometrical area of the

electrode. The electrochemical impedance spectroscopy (EIS) measurements were

recorded in a frequency range from 0.01 Hz to 100 kHz at an open circuit potential. The

product (CO and H_2) concentration in the outlet gases was analyzed through an on-line

gas chromatography (GC, Panna A91Plus). The Faradaic efficiency of CO (FE_{CO}) and

H_2 (FE_{H2}) were calculated using eq. (2):

$$FE = \frac{n \times z \times F}{Q} \qquad (2)$$

where n represent the number of electrons transferred to certain product (2 for CO and

H_2), *z* is the amount of gas generated (CO and H_2), F is the Faraday constant (96485

$C \cdot mol^{-1}$) and Q is the total charge passed over a given time of analysis.

Turnover frequency (TOF, h^{-1}) for CO production was calculated using eq. (3).

$$TOF = \frac{j_{CO}/zF}{m_{cat}w_{Ni}/M_{Ni}} \times 3600 \tag{3}$$

where j_{CO} is the partial current density of CO ($A \cdot cm^{-2}$), m_{cat} indicates the catalyst mass loaded in the electrode (g), w_{Ni} denotes the total weight percent of Ni in the catalyst (wt%) measured from AAS and M_{Ni} is the atomic mass of Ni (58.69 $g \cdot mol^{-1}$).

3. Results and discussion

The Ni-N-C-NH4Cl was prepared by the NH4Cl-assited pyrolysis method, as demonstrated in Fig. 1a. Briefly, the g-C3N4 nanosheets were first synthesized from melamine and acted as precursor and template for the synthesis of sheet-like catalyst. Microscopic images showed an ultrathin wrinkled sheet-like morphology (Fig. S1) with a thickness of only 1.15 nm (Fig. S2). X-ray diffraction (XRD) patterns presented two distinct diffraction peaks corresponding to the (100) and (002) planes of g-C3N4 (Fig. S3) [28]. Such a sheet-like structure is highly beneficial for the subsequent Ni^{2+} and glucose adsorption [29]. During hydrothermal process, the Ni^{2+} was first chemically adsorbed on the interior surface of g-C3N4 nanosheets, forming a g-C3N4 coordinated Ni scaffold (Ni-g-C3N4). Meanwhile, glucose underwent polymerization and carbonization, turning into carbon particles accumulated on the surface of Ni-g-C3N4 to form ternary Ni-g-C3N4@C catalysts. Some non-adsorbed carbon particles can be washed by the following centrifugation. The counterpart sample without Ni introduction was prepared

and denoted as g-C$_3$N$_4$@C. Notably, the crystalline structure (Fig. S3) of g-C$_3$N$_4$@C and Ni-g-C$_3$N$_4$@C almost unchanged after hydrothermal reaction. The slight shift of (002) diffraction peak from 27.4° of g-C$_3$N$_4$ to 27.7° of g-C$_3$N$_4$@C and Ni-g-C$_3$N$_4$@C may be due to the overlap of the (002) plane between amorphous carbon and g-C$_3$N$_4$. Both g-C$_3$N$_4$@C and Ni-g-C$_3$N$_4$@C precursors showed similar nanosheet morphologies (Fig. S4 and S5) to amorphous carbon deposited on the surface apparently. The lattice fringes of Ni-based species were not observed due to the carbon blocking. In the subsequent pyrolysis and acid leaching process, the prepared Ni-g-C$_3$N$_4$@C was mixed with NH$_4$Cl and converted to the mesoporous Ni-N-C-NH$_4$Cl catalyst. During this process, Ni-g-C$_3$N$_4$@C was decomposed and converted to Ni-N-C structure. Meantime, the released bountiful NH$_3$ and HCl gases from NH$_4$Cl acted as heteroatom sources to optimize the mesopore size and increase the N doping content. Besides, the carbon layer derived from glucose on the surface of Ni-g-C$_3$N$_4$ could effectively inhibit the migration of Ni atoms and maintain the Ni-N$_x$ sites. To validate the roles of single Ni sites and NH$_4$Cl on CO$_2$RR performance, additional two control samples of N-C and Ni-N-C were also prepared under similar conditions except for no addition either both NiCl$_2$·6H$_2$O and NH$_4$Cl or just NH$_4$Cl.

As presented by field-emission scanning electron microscopy (FESEM) and transmission electron microscopy (TEM) images (Fig. 1b and 1c), the as-prepared Ni-N-C-NH$_4$Cl catalyst presented an ultrathin porous nanosheet-like morphology with wrinkled surfaces, which was analogous to those observed for N-C (Fig. S6) and Ni-N-C

(Fig. S7). No distinct Ni-based nanoclusters or nanoparticles were noted in the images, suggesting the complete removal of the Ni-based nanoclusters and nanoparticles after acid leaching, leaving only single Ni atoms in the ionic state. This observation can be confirmed by the absence of patterns related to Ni-based species in the selected area electron diffraction (SAED) patterns (Fig. S8), which showed only carbon diffraction with poor crystallinity. The atomic force microscopy (AFM) image presented that the thickness of the nanosheets was only about 3.3 nm (Fig. S9). Aberration-corrected high-angle annular dark-field scanning transmission electron microscopy (AC-HAADF-STEM) image revealed that individual Ni atoms were dispersed on the carbon nanosheets (Fig. 1d). EDS elemental mapping images indicated the uniform distributions of the Ni, N and C elements in the Ni-N-C-NH$_4$Cl catalyst (Fig. 1e). The actual content of Ni elements in the Ni-N-C-NH$_4$Cl measured by the atomic absorption spectroscopy (AAS) was about 1.69 wt% (Table S1). These results convinced the successful preparation of such ultrathin nanosheet catalyst with abundant Ni sites dispersed at the atomic level.

The XRD diffraction peaks (Fig. 2a) show a low graphitization degree of prepared catalysts with only one broad peak at about 24° for the (002) planes of carbon [30]. No peaks related to Ni-based metal or compounds can be observed, consistent with the TEM characterizations. Raman spectra (Fig. 2b) show two distinct peaks of D and G bands of carbon at approximately 1336 and 1590 cm^{-1} [31]. The D band was attributed to the disordered and amorphous carbon network, and the D/G intensity ratio (I_D/I_G) could

reflect the defect degree of the carbon structure [32]. By contrast, Ni-N-C-NH4Cl showed a higher I_D/I_G value (1.041), indicating its higher defect degree induced by NH4Cl co-pyrolysis. Meanwhile, the TG analyses (Fig. S10) conducted under air atmosphere also confirmed more structural defects generated in Ni-N-C-NH4Cl catalyst, as indicated by a much lower oxidation temperature [33]. The observed little residual above 600 °C was mainly ascribed to the NiO originating from the oxidation of doped Ni species [34]. The Ni loading calculated from the residual signified a much higher Ni content (2.36 wt%) of the Ni-N-C-NH4Cl catalyst than that of the Ni-N-C (1.12 wt%), in accordance with the AAS results (Table S1). The N_2 adsorption-desorption isotherms (Fig. 2c) indicated a mesoporous structure of the prepared catalysts, showing a typical type IV of hysteresis loop [35]. Although with a smaller specific surface area of Ni-N-C-NH4Cl (Table S2), it exhibited more distinct mesopores in the range of 7-10 nm (Fig. 2d), which has been reported to be beneficial to CO_2 transfer and adsorption in the humid environment [36]. To verify the conclusion, CO_2 temperature-programmed desorption (CO_2-TPD) analyses of Ni-N-C and Ni-N-C-NH4Cl were conducted (Fig. S11). The observed significantly larger desorption peak area of the Ni-N-C-NH4Cl confirmed its stronger capability for CO_2 adsorption and enhanced local CO_2 concentration. These observations demonstrated the unique pore modulation capability of NH_3 and HCl gas decomposed from NH4Cl.

The chemical structure and surface composition of prepared catalysts were disclosed by X-ray photoelectron spectroscopy (XPS) analysis. The full XPS survey

spectrum indicated the coexistence of Ni, N, C and O elements in the catalysts (Fig. S12).

The high-resolution N 1s spectra (Fig. 2e) could be deconvoluted into four peaks, attributing to pyridinic N (398.3 eV), pyrrolic N (400.6 eV), graphitic N (402.6 eV) and oxidized N (403.8 eV), respectively [37]. The new peak at 399.3 eV indicated the formation of Ni-Nx structure [37]. In comparison with that for N-C, the binding energies of pyridinic N shifted to a lower value for Ni-N-C and Ni-N-C-NH4Cl catalysts, which may be ascribed to the coordination between Ni atoms and pyridinic N [38]. In particular, pyrrolic N was predominant in the N-C and Ni-N-C samples. After NH4Cl assisted pyrolysis, the content of pyridinic N increased distinctly and took up the largest portion (3.54 wt%) in the derived Ni-N-C-NH4Cl catalyst (Fig. 2f and Table S3), convincing its higher capability to coordinate Ni atoms and form more Ni-Nx sites in the catalyst [39]. Such phenomena confirmed the effectiveness of NH4Cl in improving the doping content of pyridinic N species during pyrolysis. The prepared Ni-N-C-NH4Cl also possessed the highest Ni content of up to 3.33 wt% (Fig. 2f). Deconvolution of the Ni 2p spectra of Ni-N-C and Ni-N-C-NH4Cl presented two major peaks of Ni $2p_{3/2}$ and Ni $2p_{1/2}$ at about 855.1 and 873.1 eV accompanied with two shakeup satellites at 861.4 and 879.7 eV (Fig. S13), which corresponded to the Ni^{n+} (0<n<2) in the structure of Ni-Nx moieties. No peak related to metallic Ni^0 at approximately 853 eV was observed [40]. These results suggested that the Ni species in these catalysts were atomically dispersed in the form of Ni-Nx sites instead of aggregated Ni nanoparticles, in accordance with the XRD and TEM analyses. A comparison of the Ni content determined by AAS, TG and XPS (Fig.

S14) indicated a high density and exposure of single Ni sites in the Ni-N-C-NH4Cl catalyst.

To further probe the valence state and coordination structure of Ni atoms, the X-ray absorption near edge structure (XANES) and the extended X-ray absorption fine structure (EXAFS) spectra of Ni-N-C-NH4Cl were conducted using Ni foil and NiO as contrasting samples. As observed in Fig. 3a, the absorption edge position of Ni-N-C-NH4Cl was located between those of Ni foil and NiO, indicating that the Ni atoms in the catalyst have a valence state situated between 0 and +2 [41]. The Fourier transformed EXAFS (Fig. 3b) obtained from the k^3 $x(k)$ functions (Fig. S15) presented one prominent peak centered at 1.4 Å, which corresponded to the Ni-N scattering path. Similar results were observed in the wavelet transform (WT) programs of Ni-N-C-NH4Cl (Fig. 3c) catalyst. The contour plots of catalyst exhibited the WT maximum at about 6.0 Å, which was ascribed to the Ni-N coordination in comparison with Ni foil and NiO.

The EXAFS fitting curve (Fig. 3d and 3e) proved that each Ni atom in the Ni-N-C-NH4Cl was mainly coordinated by four N atoms to form the Ni-N4 active sites and the average bond length was 1.85 Å (Table S4). Consequently, these observations were in good accordance with the AC-HAADF-STEM and XPS analyses, collectively indicating that the Ni-N-C-NH4Cl has an optimized mesopore size (7-10 nm), significantly higher contents of Ni-N4 and pyridinic N sites on the carbon nanosheets, which could be advantageous to its CO2RR performance.

14

CO$_2$RR was conducted in a H-type electrochemical cell containing 0.5 M KHCO$_3$ electrolyte. Only gas products of CO and H$_2$ were detected, and the total Faradaic efficiency for CO and H$_2$ was measured to be approximately 100% under all applied potentials. The electrocatalytic activity was first investigated by the linear sweep voltammetry (LSV) curves in the potential range from 0 to −0.8 V *vs*. RHE. As demonstrated in Fig. 4a, the Ni-N-C-NH$_4$Cl catalyst exhibited a much larger current density in the CO$_2$-saturated solution than that in the Ar-saturated one, confirming its good activity for CO$_2$RR. Similar observations can be noted in other carbon electrocatalysts [42, 43].

Moreover, the LSV curves showed that the Ni-N-C-NH$_4$Cl has a significantly larger current response (-17 mA·cm^{-2} at −0.8 V *vs*. RHE) and more positive onset potential (about -0.4 V *vs*. RHE) than those of N-C and Ni-N-C catalysts (Fig. 4b), implying its superior catalytic capability for CO$_2$RR to CO. The Faradaic efficiency (FE$_{CO}$) and partial catalytic current density for CO (j_{CO}) measured from the potentiostatic electrolysis experiments (Fig. S16) are illustrated in Fig. 4c and 4d. The Ni-N-C-NH$_4$Cl showed a better selectivity with the maximum FE$_{CO}$ as high as 98% at a small potential of −0.62 V *vs*. RHE, and maintained over 80% in the wide potential range from −0.42 to −0.72 V *vs*. RHE (Fig. 4c). While for the N-C and Ni-N-C samples, the peak values of FE$_{CO}$ are only 29% and 78%, respectively, revealing that the NH$_4$Cl co-pyrolysis was beneficial to the selectivity for CO formation. Accordingly, FE$_{H2}$ for all catalysts showed quite the opposite tendency (Fig. S17). In addition, Ni-N-C-NH$_4$Cl catalyst also

demonstrated the highest j_{CO} of 8.5 mA·cm^{-2} at the highest point of Faraday efficiency of −0.62 V *vs*. RHE, that is, the overpotential is as low as 510 mV (Fig. 4d).

Besides, the Ni-N-C-NH$_4$Cl catalyst also showed good electrocatalytic stability with an activity decay lower than 5% (Fig. 4e). After the long-term potentiostatic electrolysis, the morphology (Fig. S18) and the LSV curve (Fig. S19) remained almost unchanged compared with those before the stability test, further confirming the good stability of the Ni-N-C-NH$_4$Cl catalyst. These results presented here indicated the high catalytic performance of the Ni-N-C-NH$_4$Cl catalyst at low potentials, which is comparable to many previously reported CO$_2$RR eletrocatalysts (partially listed in Fig. 4f and Table S5).

To elucidate the superior performance of Ni-N-C-NH$_4$Cl, the electrochemically active surface area (ECSA) was estimated from the double-layer capacitance (C$_{dl}$) that was obtained from CV curves at different scan rates (Fig. 5a and S20) [44, 45]. Clearly, the C$_{dl}$ of Ni-N-C-NH$_4$Cl (15.3 mF·cm^{-2}) was much larger than those of N-C (5.1 mF·cm^{-2}) and Ni-N-C (8.3 mF·cm^{-2}), indicative of its larger exposure of the active sites for CO$_2$RR [46]. Contact angle measurement (Fig. S21) showed a hydrophobic property and then a higher affinity with CO$_2$ than H$_2$O molecules for Ni-N-C-NH$_4$Cl, which was beneficial for CO$_2$RR.

Additionally, the calculated larger turnover frequency (TOF) of 3885 h^{-1} at -0.62 V *vs*. RHE convinced the higher intrinsic activity of the Ni-N-C-NH$_4$Cl catalyst (Fig. 5b). To understand the reaction kinetics of CO$_2$RR, the electrochemical impedance

spectroscopy (EIS) was performed for investigated catalysts. Specifically, Ni-N-C-NH4Cl presented a much lower charge-transfer resistance (Fig. S22), which was beneficial for the formation of intermediates during CO2RR procedure. The favorable reaction kinetics of Ni-N-C-NH4Cl can also be well probed by the smaller Tafel slop (90 mV·dec^{-1}), indicating the NH4Cl-assisted pyrolysis can accelerate the reaction kinetics of CO2RR process (Fig. 5c). The result also implied that the rate-determining step in CO2RR was the transfer of the first electron, which rendered the transformation of *CO2 to a *CO2$^-$ intermediate [12, 47]. Therefore, the stabilization of *CO2$^-$ was significant to improve CO2RR process.

To evaluate the binding strength of *CO2$^-$, oxidative LSV curves (Fig. 5d) in N2-saturated 0.1 M KOH electrolyte were conducted by employing the OH$^-$ as a representative for *CO2$^-$ [12, 47]. The potential for OH$^-$ adsorption over Ni-N-C-NH4Cl was more negative than the controlled catalysts, which meant a more stronger binding strength with *CO2$^-$ intermediate and then an accelerated electro-chemical reduction process. The above descriptions indicated the advantages of the derived Ni-N-C-NH4Cl catalyst for CO2RR.

To unveil the effect of NH4Cl co-pyrolysis on the property and CO2RR performance of catalyst, the counterparts with different NH4Cl addition were investigated and denoted as Ni-N-C-1 and Ni-N-C-3 by changing the mass ratio of Ni-g-C3N4@C and NH4Cl to 1:1 and 3:1. The Ni loadings of Ni-N-C-1 and Ni-N-C-3 obtained from AAS were 1.06 and 1.15 wt% (Table S2), respectively. All samples exhibited similar diffraction patterns

17

(Fig. S23), showing only one diffraction peak at 24°. The defect degree estimated from Raman spectra (Fig. S24) showed the larger I_D/I_G value of Ni-N-C-NH$_4$Cl catalyst, indicating moderate NH$_4$Cl addition could introduce more defect in the carbon nanosheets. Correspondingly, the Ni-N-C-NH$_4$Cl showed the highest catalytic performance (both FE$_{CO}$ and j_{CO}) over the whole potential range, thus convincing the optimal NH$_4$Cl addition for more efficient and selective electroreduction of CO$_2$ to CO (Fig. S25).

To elucidate the active site of Ni-N-C-NH$_4$Cl catalyst for CO$_2$RR, the electrolyte was first added with 10 mM KSCN to poison the Ni-N$_4$ sites of catalyst. As presented in Fig. 6a, both the j_{CO} and FE$_{CO}$ of Ni-N-C-NH$_4$Cl catalyst dropped distinctly with KSCN treatment. The apparent decrease in catalytic performance could be ascribed to the poison of Ni-N$_4$ sites by SCN ions [48], signifying that the atomically dispersed Ni are the active sites for CO$_2$RR. Similar results have been verified by many published works [49-51].

To further examine the influence of pyridinic N on CO$_2$RR performance, phosphate anions were applied to selectively block the pyridinic N species [16]. As demonstrated in Fig. 6b, the FE$_{CO}$ of Ni-N-C-NH$_4$Cl decreased slightly with prolonging the soaking time in H$_3$PO$_4$, while the j_{CO} dropped apparently, indicating that pyridinic N indeed has a promotion effect on CO$_2$RR. This observation was consistent with other reports, which demonstrated the important role of pyridinic N in promoting CO$_2$ adsorption and intermediate *COOH formation [52].

18

Based on the above discussion and reported results [53, 54], the possible reaction mechanism for CO_2RR to CO over prepared catalysts was proposed, as illustrated in Fig. 6c. One CO_2 molecule was first adsorbed by Ni-N_4 active sites and captured an initial electron to form the adsorbed $*CO_2^-$ intermediate. Then, $*COOH$ was generated after accepting one proton. Meanwhile, the existence of abundant pyridinic N contributed to the adsorption of CO_2 molecules and the formation of $*COOH$ intermediates [53]. Afterwards, $*COOH$ further took a proton and an electron to generate the adsorbed $*CO$ and H_2O. Finally, the main product CO was desorbed as CO gas due to the weak interaction between the formed $*CO$ intermediate with Ni-N_4 sites ($*$ represented the intermediates that bonded with Ni-N_4).

4. Conclusion

In summary, mesoporous ultrathin sheet-like electrocatalysts with abundant Ni-N_4 active sites have been successfully created by a novel NH_4Cl-assited pyrolysis technology. Benefiting from its optimized mesopore size (7-10 nm), increased concentrations of single Ni active sites (3.33 wt%) and pyridinic N species (3.54 wt%), this catalyst exhibits excellent catalytic performance for CO_2RR. The maximum FE_{CO} is as high as 98% at a low overpotential of -0.62 V *vs*. RHE with the j_{CO} of 8.5 mA·cm^{-2}. Particularly, the FE_{CO} can be maintained above 80% in a wide potential range from -0.43 to -0.73 V. Experimental observations confirm the decisive role of Ni-N_4 sites and the promotion effect of pyridinic N species in catalyzing CO_2RR. This work brings new insights in the preparation of high-performance M-N-C catalyst, an alternative for the

19

noble metal catalysts, for various electrochemical applications.

Acknowledgements

References

[1] J. Han, X.M. Deng, K.Y. Chen, S. Imhanria, Y. Sun, W. Wang, Renew. Energy 177 (2021) 636-642.

[2] L. Ye, Y. Ying, D. Sun, Z. Zhang, L. Fei, Z. Wen, J. Qiao, H. Huang, Angew. Chem. Int. Ed. 59 (2020) 3244-3251.

[3] M. Tahir, B. Tahir, J. Mater. Sci. Technol. 106 (2022) 195-210.

[4] W. Chen, Z.L. Fan, X.L. Pan, X.H. Bao, J. Am. Chem. Soc. 130 (2008) 9414-9419.

[5] D. Ping, S.G. Huang, S.D. Wu, Y.F. Zhang, F. Yi, L.F. Han, S.W. Wang, H. Wang, X.Z. Yang, D.J. Guo, J. Hao, S.M. Fang, Int. J. Hydrog. Energy 47 (2022) 23653-23660.

[6] M. Abdinejad, C. Dao, X.A. Zhang, H.B. Kraatz, J. Energy Chem. 58 (2021) 162-169.

[7] X.L. Lu, T.S. Yu, H.L. Wang, L.H. Qian, R.C. Luo, P. Liu, Y. Yu, L. Liu, P.X. Lei , S.L. Yuan, J. Mater. Sci. Technol. 43 (2020) 154-160.

[8] X. Min, M.W. Kanan, J. Am. Chem. Soc. 137 (2015) 4701-4708.

[9] Q. Lu, J. Rosen, Y. Zhou, G.S. Hutchings, Y.C. Kimmel, J.G. Chen, F. Jiao, Nat.

Commun. 5 (2014) 3242.

[10] S.D. Wu, F. Yi, D. Ping, S.G. Huang, Y.F. Zhang, L.F. Han, S.W. Wang, H. Wang, X.Z. Yang, D.J. Guo, G.J. Liu, S.M. Fang, Carbon 196 (2022) 1-9.

[11] Y. Lu, H.J. Wang, P.F. Yu, Y.F. Yuan, R. Shahbazian-Yassar, Y. Sheng, S.Y. Wu, W.G. Tu, G.Y. Liu, M. Kraft, R. Xu, Nano Energy 77 (2020) 105158.

[12] Z.P. Chen, X.X. Zhang, W. Liu, M.Y. Jiao, K.W. Mou, X.P. Zhang, L.C. Liu, Energy Environ. Sci. 14 (2021) 2349-2356.

[13] C. Jia, X. Tan, Y. Zhao, W.H. Ren, Y.B. Li, Z. Su, S.C. Smith, C. Zhao, Angew. Chem. Int. Ed. 60 (2021) 23342-23348.

[14] A. Razmjoo, L.G. Kaigutha, M.A.V. Rad, M. Marzband, A. Davarpanah, M. Denai, Renew. Energy 164 (2021) 46-57.

[15] C. Zhang, Z.H. Fu, Q. Zhao, Z.J. Du, R.F. Zhang, S.M Li, Electrochem. Commun. 116 (2020) 106758.

[16] S. Liu, H.B. Yang, X. Huang, L.H. Liu, W.Z. Cai, J.J. Gao, X.N. Li, T. Zhang, Y.Q. Huang, B. Liu, Adv. Funct. Mater. 28 (2018) 1800499.

[17] L. Zhang, J. Xiong, Y.H. Qin, C.W. Wang, Carbon 150 (2019) 475-484.

[18] D.W. Xi, J.Y. Li, J.X. Low, K.K. Mao, R. Long, J.W. Li, Dai, Z.H. T.Y. Shao, Y. Zhong, Y. Li, Z.B. Li, X.J. Loh, S. Li, E.Y. Ye, Y.J. Xiong, Adv. Mater. (2021) 2104090.

[19] Y. Wang, X.B. Zheng, D.S. Wang, Nano Res. 15 (2022) 1730-1752.

[20] R.Z. Li, D.S. Wang, Nano Res. 15 (2022) 6888-6923.

[21] B. Hu, X.B. Zhu, X.H. An, C.X. Wang, X.B. Wang, J.L. He, Y Zhao, Inorg. Chem.

59 (2020) 17134-17142.

[22] H.J. Wang, G.Y Liu, C.P. Chen, W.G. Tu, Y. Lu, S.Y. Wu, D. O'Hare, R. Xu, ACS Sustainable Chem. Eng. 9 (2021) 3785-3794.

[23] H.P. Yang, Q. Lin, C. Zhang, X.Y. Yu, Z. Cheng, G.D. Li, Q. Hu, X.Z. Ren, Q.L. Zhang, J.H. Liu, C.X. He, Nat. Commun. 11 (2020) 593.

[24] S.G. Han, D.D. Ma, S.H. Zhou, K.X. Zhang, W.B. Wei, Y.H. Du, X.T. Wu, Q. Xu, R.Q. Zou, Q.L. Zhu, Appl. Catal. B-Environ. 283 (2021) 119591.

[25] Y.X. Li, S.L. Zhang, W.R. Cheng, Y. Chen, D.Y. Luan, S.Y. Gao, X.W. Lou, Adv. Mater. 34 (2021) 2105204.

[26] X.G. Li, W.T. Bi, M.L. Chen, Y.X. Sun, H.X. Ju, W.S. Yan, J.F. Zhu, X.J. Wu, W.S. Chu, C.Z. Wu, Y. Xie, J. Am. Chem. Soc. 139 (2017) 14889-14892.

[27] R. Daiyan, X. Zhu, Z. Tong, L. Gong, A. Razmjou, R.S.Liu, Z. Xia, X. Lu, L. Dai, R. Amal, Nano Energy 78 (2020) 105213.

[28] S.Q. Sun, Y.C. Wu, J.F. Zhu, C.J. Lu, Y. Sun, Z. Wang, J. Chen, Chem. Eng. J. 427 (2022) 131032.

[29] Y.H. Cao, Y.Q. Zhu, C.L. Du, X.Y. Yang, T.Y. Xia, X.L. Ma, C.B. Cao, ACS Nano 16 (2022) 1578-1588.

[30] S.D. Wu, X.N. Lv, D. Ping, G.W. Zhang, S.W. Wang, H. Wang, X.Z. Yang, D.J. Guo, S.M. Fang, Electrochim. Acta 340 (2020) 135930.

[31] A.C. Ferrari, D.M. Basko, Nat. Nanotechnol. 8 (2013) 235-246.

[32] U.N.T. Nguyen, D.V. Lam, H.C. Shim, S.M. Lee, Renew. Energy 17 (2021)

116-123.

[33] Q.H. Wang, Y.W. Li, N. Liao, X.F. Xu, S.B. Sang, Y.B. Xu, G.H. Wang, M. Nath, Ceram. Int. 43 (2017) 16710-16721.

[34] S.Y. Zhao, Y. Cheng, J.P. Veder, B. Johannessen, M. Saunders, L.J. Zhang, C. Liu, M.F. Chisholm, R. De Marco, J. Liu, ACS Appl. Energy Mater. 1 (2018) 5286−5297.

[35] W. Younas, M. Naveed, C.B. Cao, Y.Q. Zhu, C.L. Du, X.L. Ma, N. Mushtaq, M. Tahir, M. Naeem, J. Colloid Interface Sci. 608 (2022) 1005-1014.

[36] W.F. Xiong, H.F. Li, H.M. Wang, J.D. Yi, H.H. You, S.Y. Zhang, Y. Hou, M.N. Cao, T. Zhang, R. Cao, Small 16 (2020) 2003943.

[37] C. Wang, X. Hu, X.S. Hu, X.Y Liu, Q.X. Guan, R. Hao, Y.P. Liu, W. Li, Appl. Catal. B-Environ. 296 (2021) 120331.

[38] M Jia, C Choi, T.S. Wu, M. Chen, Z Sun, Chem. Sci. 9(2018) 8775-8780

[39] Z.P. Miao, Y. Xia, J.S. Liang, L.F. Xie, S.Q. Chen, S.Z. Li, H.L. Wang, S. Hu, J.T. Han, Q. Li, Small 17 (2021) 2100735.

[40] C.J. Lei, Y. Wang, Y. Hou, P. Liu, J. Yang, T. Zhang, X.D. Zhuang, M.W. Chen, B. Yang, L.C. Lei, C. Yuan, M. Qiu, X.L. Feng, Energy Environ. Sci. 12 (2019) 149-156.

[41] Y.Z. Li, B. Wei, M.H. Zhu, J. Chen, Q.K. Jiang, B. Yang, Y. Hou, L.C. Lei, Z.J. Li, R.F. Zhang, Y.Y. Lu, Adv. Mater. 33 (2021) 2102212.

[42] Y.M. Liu, S. Chen, X. Quan, H.T. Yu, J. Am. Chem. Soc. 137 (2015) 11631-11636.

[43] Z. Zhang, L. Yu, Y.C. Tu, R.X. Chen, L.H. Wu, J.F. Zhu, D.H. Deng, Cell Rep. Phys. Sci. 1 (2020) 100145.

[44] P.L. Lu, Y.J. Yang, J. Yao, M. Wang, S. Dilpazir, M.L. Yuan, J.X. Zhang, X. Wang, Z.J. Xie, G.J. Zhang, Appl. Catal. B-Environ. 241 (2018) 113-119.

[45] R. Daiyan, R. Chen, P. Kumar, N. Bedford, J. Qu, J. Cairney, X. Lu, R. Amal, ACS Appl. Mater. Interfaces 12 (2020) 9307-9315.

[46] S.J. Zhao, N. Xiao, H.Q. Li, Z. Guo, J.P. Bai, J. Xiao, H.D. Guo, X.Q. Ma, J.S. Qiu, J. CO_2 Util. 49 (2021) 101549.

[47] K. Liu, J. Wang, M. Shi, J. Yan,Q. Jiang, Adv. Energy Mater. 9 (2019) 1900276.

[48] X. Wang, S. Feng, W. Lu, Y. Zhao, S. Zheng, W. Zheng, X. Sang, L. Zheng, Y. Xie, Z. Li, B. Yang, L. Lei, S. Wang, Y. Hou, Adv. Func. Mater. 31 (2021) 2104243.

[49] S. Li, M. Ceccato, X. Lu, S. Frank, N. Lock, A. Roldan, X.M. Hu, T. Skrydstrup, K. Daasbjerg, J. Mater. Chem. A 9 (2021) 1583-1592.

[50] S. Yang, J. Zhang, L. Peng, M. Asgari, D. Stoian, I. Kochetygov, W. Luo, E. Oveisi, O. Trukhina, A.H. Clark, D.T. Sun, W.L. Queen, Chem. Sci. 11 (2020) 10991-10997.

[51] W. Liu, S. Wei, P. Bai, C. Yang, L. Xu, Appl. Catal. B-Environ. 299 (2021) 120661.

[52] Q. Lu, C. Chen, Q. Di, W.L. Liu, X.H. Sun, Y.X. Tuo, Y. Zhou, Y. Pan, X. Feng, L. Li, D. Chen, J. Zhang, ACS Catal. 12 (2022) 1364-1374.

[53] P.F. Hou, W.L. Song, X.P. Wang, Z.P. Hu, P. Kang, Small 16 (2020) 2001896.

[54] P. Yao, J. Zhang, Y. Qiu, Q. Zheng, H. Zhang, J. Yan, X. Li, ACS Sustainable Chem. Eng. 9 (2021) 5437-5444.

**Figures and Figure Captions**
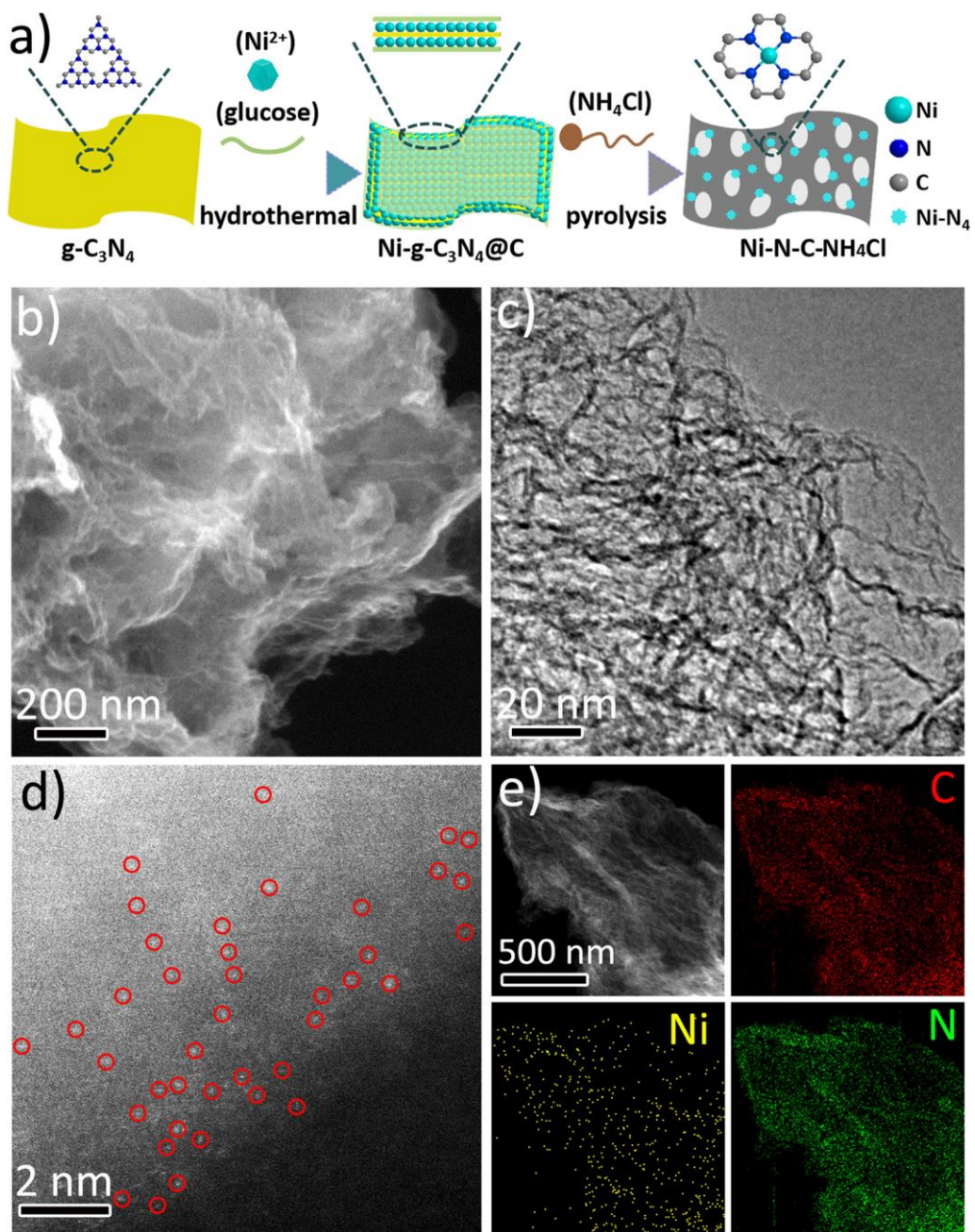
Fig. 1. (a) The fabrication scheme of Ni-N-C-NH₄Cl catalyst. (b) FESEM, (c) TEM, (d) AC-HAADF-STEM and (e) EDX element mapping images of Ni-N-C-NH₄Cl catalyst.
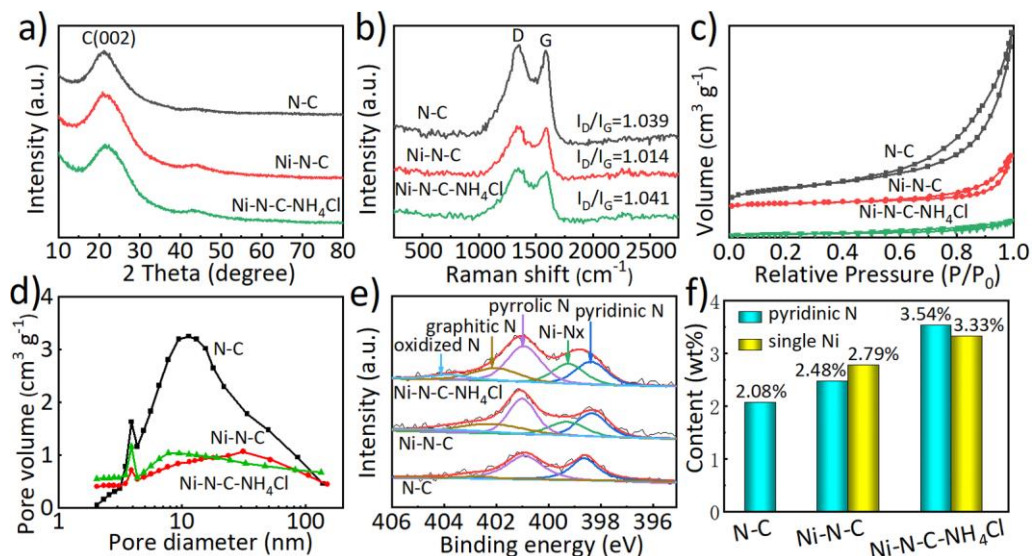
Fig. 2. (a) XRD patterns, (b) Raman spectra, (c, d) N_2 adsorption-desorption isotherms and corresponding pore size distributions of N-C, Ni-N-C and Ni-N-C-NH$_4$Cl catalysts. (e) XPS spectra of N 1s and (f) contents of pyridinic N and Ni species calculated by XPS in the N-C, Ni-N-C and Ni-N-C-NH$_4$Cl catalysts.
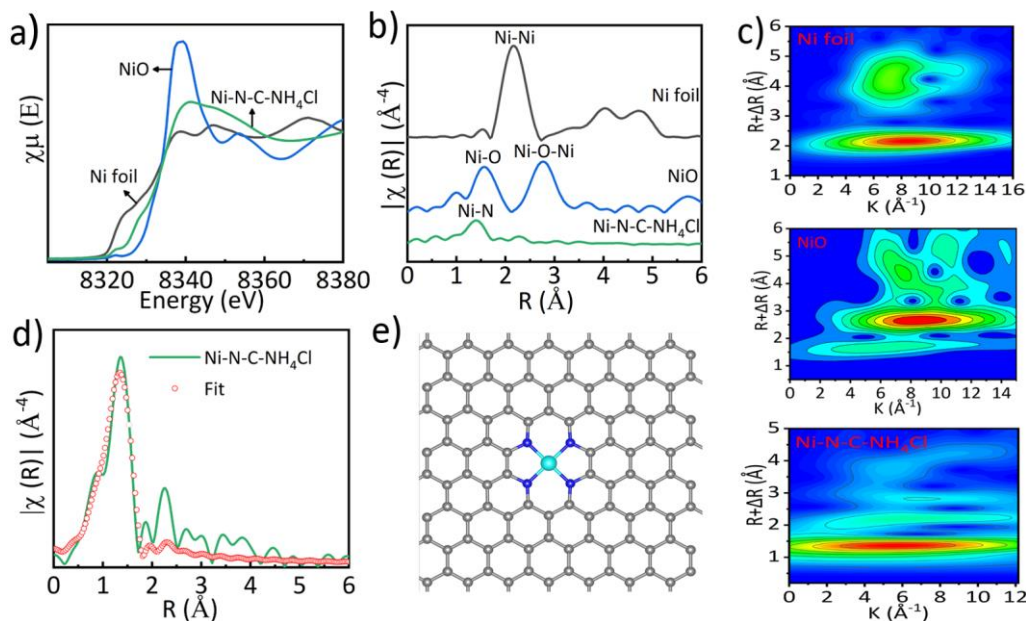

Fig. 3. The (a) Ni K-edge XANES spectra, (b) Fourier transform and (c) wavelet transform EXAFS spectra of Ni-N-C-NH$_4$Cl, Ni foil and NiO samples. (d) EXAFS

fitting curves of Ni-N-C-NH4Cl at *R* space and (e) the structure of Ni site in Ni-N-C-NH4Cl catalyst.
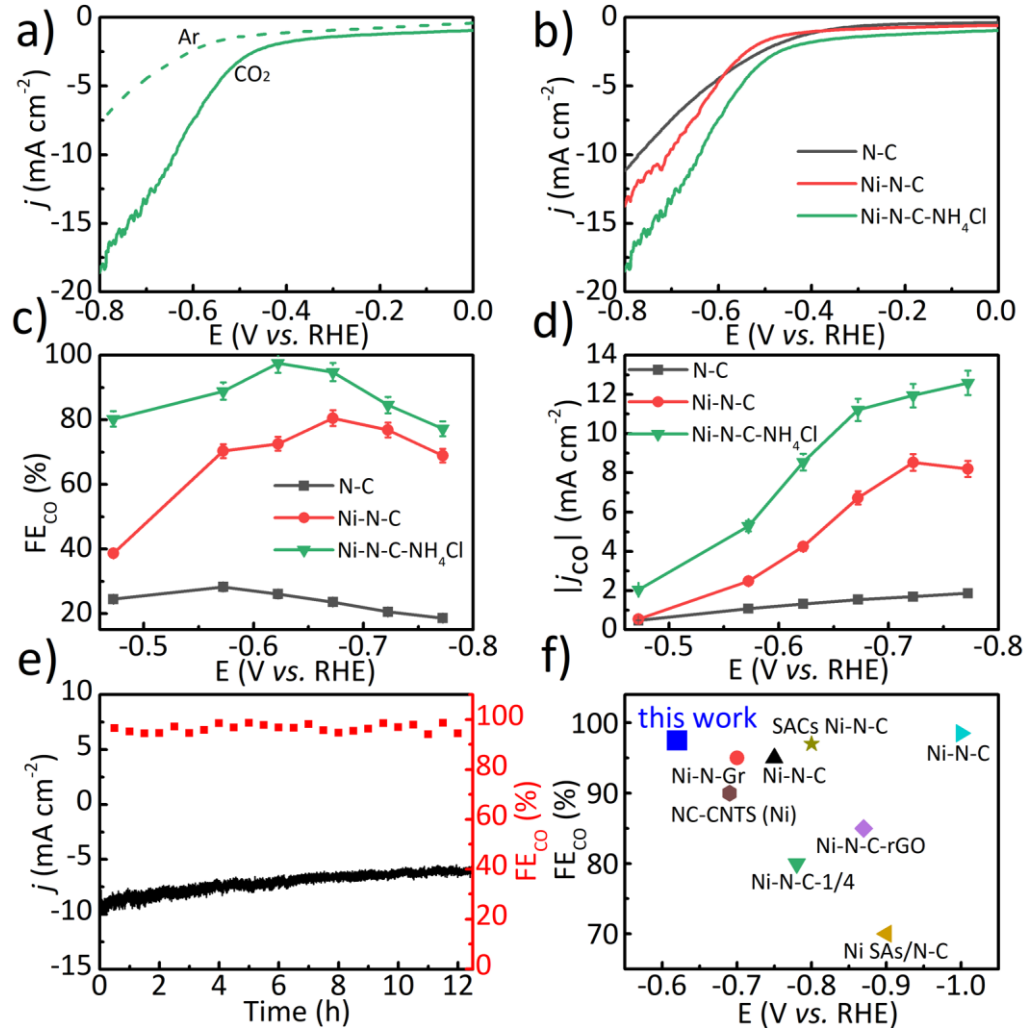
Fig. 4. (a) LSV curves of Ni-N-C-NH4Cl in 0.5 M CO2-saturated and Ar-saturated KHCO3 electrolyte, (b) LSV curves, (c) FECO and (d) *j*CO of prepared catalysts at different potentials. (e) The stability test of Ni-N-C-NH4Cl at the potential of -0.62 V *vs*. RHE. (f) Comparison of the FECO of Ni-N-C-NH4Cl and other reported catalysts for CO2RR to CO. Error bars show the fluctuations in the measured signals.
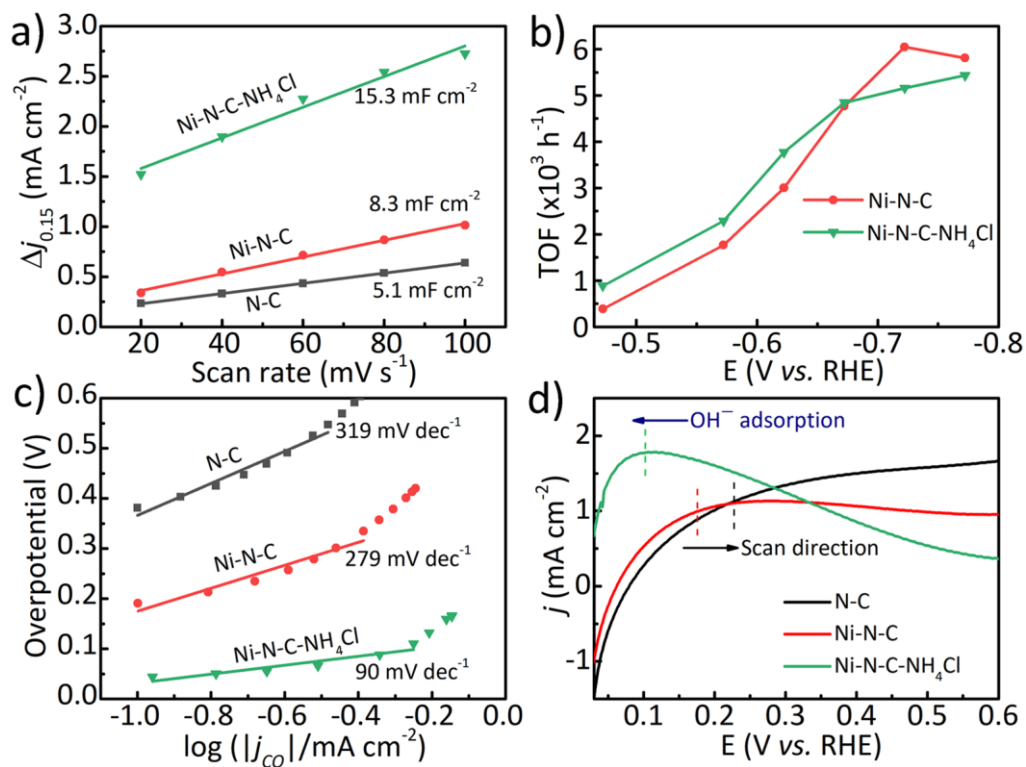
Fig. 5. The (a) capacitive current (Δj) against the scan rate at -0.15 V *vs*. RHE, (b) TOF values, (c) Tafel plots and (d) single oxidative LSV scans in N_2-saturated 0.1 mol·L^{-1} KOH of prepared catalysts.
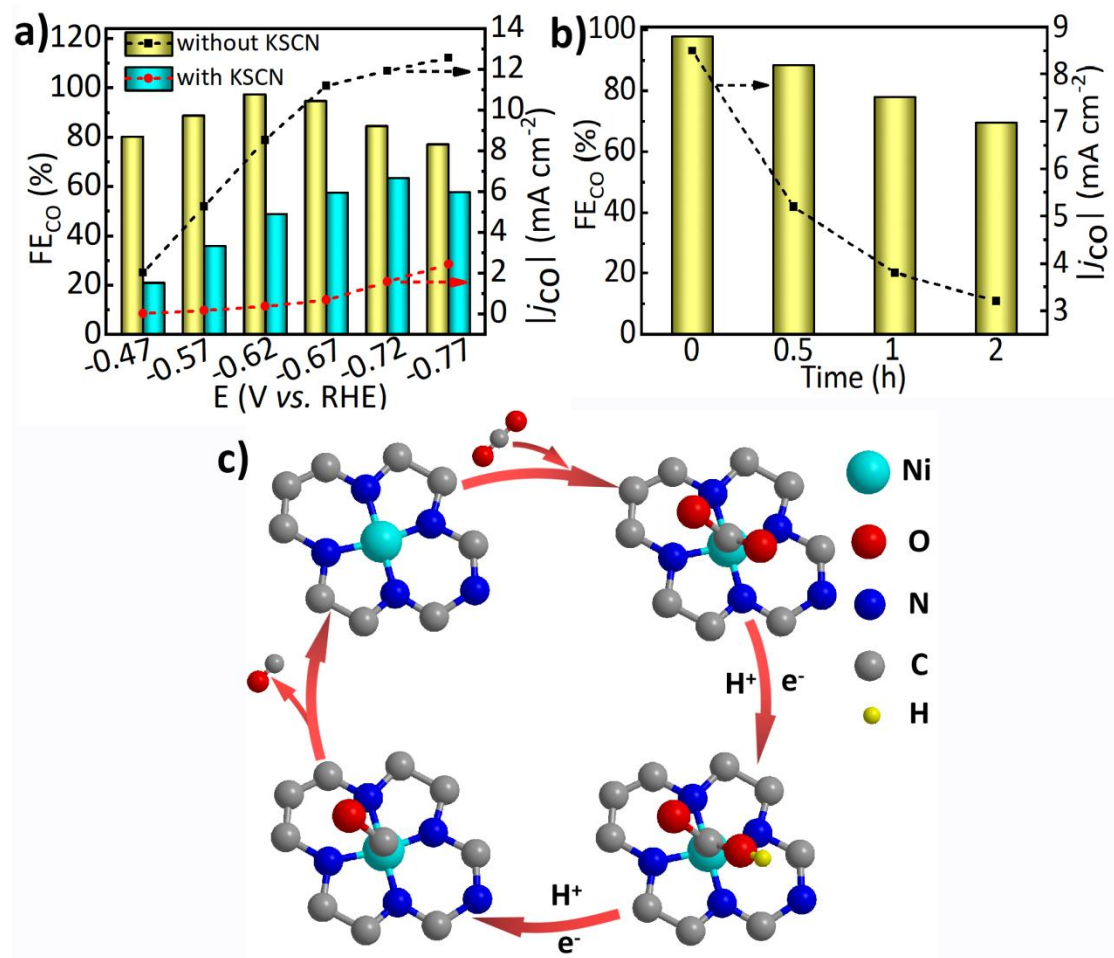
Fig. 6. The catalytic performance of Ni-N-C-NH$_4$Cl catalyst (a) with or without KSCN treatment and (b) soaked in 2 M H$_3$PO$_4$ for different times. (c) The proposed mechanism for CO$_2$ reduction to CO on Ni-N-C-NH$_4$Cl catalyst.